Commun. Comput. Phys.
doi: 10.4208/cicp.OA-2016-0050

Vol. **21**, No. 5, pp. 1258-1281
May 2017

Combined MPM-DEM for Simulating the Interaction Between Solid Elements and Fluid Particles

Youqing Yang[1,3,*], Pengtao Sun[2] and Zhen Chen[1]

[1] *Department of Civil & Environmental Engineering, University of Missouri, Columbia, MO 65211, USA.*
[2] *Department of Mathematical Sciences, University of Nevada Las Vegas, Las Vegas, NV 89154, USA.*
[3] *Department of Technology Development, Me Global Inc., Minneapolis, MN 55421, USA.*

Received 8 April 2016; Accepted (in revised version) 11 September 2016

Abstract. How to effectively simulate the interaction between fluid and solid elements of different sizes remains to be challenging. The discrete element method (DEM) has been used to deal with the interactions between solid elements of various shapes and sizes, while the material point method (MPM) has been developed to handle the multi-phase (solid-liquid-gas) interactions involving failure evolution. A combined MPM-DEM procedure is proposed to take advantage of both methods so that the interaction between solid elements and fluid particles in a container could be better simulated. In the proposed procedure, large solid elements are discretized by the DEM, while the fluid motion is computed using the MPM. The contact forces between solid elements and rigid walls are calculated using the DEM. The interaction between solid elements and fluid particles are calculated via an interfacial scheme within the MPM framework. With a focus on the boundary condition effect, the proposed procedure is illustrated by representative examples, which demonstrates its potential for a certain type of engineering problems.

AMS subject classifications: 65Z05, 76M28, 74F10

Key words: Multiphase flow, solid-fluid interaction, material point method (MPM), discrete element method (DEM).

1 Introduction

Interaction between a large number of solid elements (bodies or particles) and surrounding fluid occurs in many natural and engineering settings such as sediment transport in

*Corresponding author. *Email addresses:* yy058@mail.missouri.edu, ryang@meglobal.com (Y. Yan), pengtao.sun@unlv.edu (P. Sun), ChenZh@missouri.edu (Z. Chen)

 ©2017 Global-Science Press

https://doi.org/10.4208/cicp.OA-2016-0050 Published online by Cambridge University Press

rivers and coastal oceans, debris flows during flooding, cuttings transport in petroleum-well drilling, mineral particle size reduction in grinding mills, as well as powder handling and pneumatic conveying in pharmaceutical industries [1]. In the category of dense granular flow, the collisions between solid elements and shear drag from surrounding fluid play a dominant role. As for the study of the interaction between solid elements, discrete element method (DEM) is one of the most efficient approaches, which has found a firm place in powder mechanics and rock mechanics [2–4]. One of the key challenges of the DEM, as highlighted in a review paper by Weerasekara et al. [2], is the need for adequately simulating the fine particles in engineering applications. The fine particles represent a reasonable volume of the charge, and modify the collision and transport behaviors of the coarse particles. Due to their small size, the number of the fine particles is tremendously large, which the DEM is unable to handle.

As for the interaction between solid elements and fluid, many efforts have been made in the past based on computational fluid dynamics (CFD), such as combined DEM and moving particle semi-implicit method [5], and combined DEM and CFD [6–9]. The smoothed-particle hydrodynamics (SPH) method has been developed to simulate the motion of fluid [10, 11]. The SPH method was originally introduced to simulate the problems in astrophysics, which involve fluid particles moving arbitrarily in the absence of boundaries [12, 13]. One type of combined DEM-SPH simulation is based on one-way coupling, namely, one phase contributing to the motion of others while the reaction from others is ignored [14, 15]. Recent research focus has been on the two-way coupling [16, 17]. The verification and validation of the combined DEM-SPH has been recently conducted [18]. However, the SPH solution is unstable or not convergent in some cases [19,20]. Hence, further improvement is required on the SPH, or an alternative approach must be found.

It is proposed in this paper that the material point method (MPM) be combined with the DEM to simulate the interaction between solid elements of different sizes and surrounding fluid particles. The MPM is an extension of the particle-in-cell (PIC) method in CFD to the field of computational solid dynamics (CSD), and is a particle method formulated with the same weak formulation as that used for the finite element method (FEM) [21]. Because the deformation history is recorded with material points for history-dependent constitutive equations, the MPM is able to handle the problems with large deformation, failure evolution and multi-phase interactions, such as impact, penetration, perforation, and fluid-structure interaction with strong shocks, as demonstrated in previous studies [22–31]. In addition, the MPM has been combined with the FEM to improve the computational efficiency [32]. Another approach to improve the computational efficiency is to combine the MPM with the adaptive mesh refinement (AMR) techniques. This approach has been adopted to simulate fluid-structure interaction problems [33]. The MPM has also been employed in multi-scale simulation [34]. By taking advantages of both the MPM and DEM, hence, an effective spatial discretization procedure might be designed to better simulate the interactions among various kinds of solid elements with surrounding fluid particles.

https://doi.org/10.4208/cicp.OA-2016-0050 Published online by Cambridge University Press

It is worthy to be aware the difference between the MPM and the SPH. The MPM is developed to seek a numerical solution based on a week form of the differential equations, similar to Finite Element Method. Shape functions are used to complete interpolation and gradient operation. The SPH is a particle based method and kernel functions are utilized to calculate the interpolation and gradient.

The remaining part of this paper is organized as follows. In Section 2, we derive the equations that govern the physical process considered. The discretization with a corresponding algorithm is then laid out in Section 3. The proposed procedure is verified with three representative examples in Section 4. Finally, the concluding remarks and future work are given in Section 5.

2 Governing equations

Let θ be the volume fraction of the fluid, ρ_f the density of the fluid, and $\boldsymbol{u}_f$ the velocity of the fluid. The fluid phase is continuous and the solid phase is discrete. Take a free body diagram shown in Fig. 1. Let the fluid section of boundary be A_f, the boundary crossing the solid particles be A_p, the surface of solid particles inside the control volume V be Σ, and the surface of solid particles crossing boundary be Σ'.

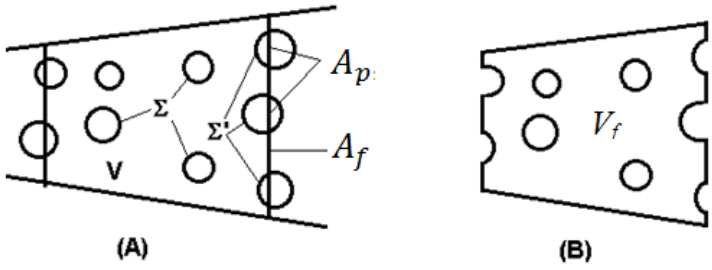


Figure 1: (A) Control volume V with fluid and particles, (B) Fluid volume V_f, excluding solid volume; modified after [35].

2.1 Continuity equations

Applying mass conservation law for the fluid inside a control volume V with boundary A, in the case where no fluid is generated or consumed, one gets

$$\frac{\partial}{\partial t}\int_V \theta\rho_f dV + \int_A (\theta\rho_f \boldsymbol{u}_f)\cdot \boldsymbol{n} dA = 0,$$

where $\boldsymbol{n}$ denotes the outward normal vector on the boundary of control volume V, $A = A_p + A_f$. According to the divergence theorem, the above equation can be rewritten as

$$\int_V \frac{\partial(\theta\rho_f)}{\partial t} dV + \int_V \nabla\cdot(\theta\rho_f \boldsymbol{u}_f)\, dV = 0.$$

https://doi.org/10.4208/cicp.OA-2016-0050 Published online by Cambridge University Press

Since the control volume V is arbitrary, we have

$$\frac{\partial(\theta\rho_f)}{\partial t}+\nabla\cdot(\theta\rho_f\boldsymbol{u}_f)=0 \tag{2.1}$$

which is similar with the formula of the continuous single phase in [36].

2.2 Momentum equations

Applying Newton's second law of motion to the fluid part within the control volume V, we get

$$\int_V\left(\theta\rho_f\frac{D\boldsymbol{u}_f}{Dt}\right)dV=\int_V\theta\rho_f\boldsymbol{g}dV+\int_{A_f\cup\Sigma'\cup\Sigma}\boldsymbol{\sigma}\boldsymbol{n}dA, \tag{2.2}$$

where $\boldsymbol{\sigma}$ is the stress tensor, $\boldsymbol{n}$ is the outward normal vector at A_f, or pointing to the solid particles at $\Sigma'\cup\Sigma$. The fluid pressure p, stress $\boldsymbol{\sigma}$ and deviatoric stress $\boldsymbol{\tau}$ have the following relationship.

$$\boldsymbol{\sigma}=-p\boldsymbol{I}+\boldsymbol{\tau}. \tag{2.3}$$

We break the second term on the right hand side of Eq. (2.2) by applying (2.3),

$$\int_{A_f\cup\Sigma'\cup\Sigma}\boldsymbol{\sigma}\boldsymbol{n}dA=\int_{A_f\cup A_p}\boldsymbol{\sigma}\boldsymbol{n}dA-\int_{\Sigma'\cup\Sigma}p\boldsymbol{n}dA+\int_{A_p}p\boldsymbol{n}dA+\int_{\Sigma'\cup\Sigma}\boldsymbol{\tau}\boldsymbol{n}dA-\int_{A_p}\boldsymbol{\tau}\boldsymbol{n}dA. \tag{2.4}$$

An empirical formula [9, 18, 37, 38] is used to calculate the contribution of the deviatoric stress at the solid-fluid interface:

$$\int_{\Sigma'\cup\Sigma}\boldsymbol{\tau}\boldsymbol{n}dA-\int_{A_p}\boldsymbol{\tau}\boldsymbol{n}dA=\sum_{j=1}^{m}\beta_j\left(\boldsymbol{v}_s\left(\boldsymbol{x}_j\right)-\boldsymbol{u}_f\left(\boldsymbol{x}_j\right)\right)V_j, \tag{2.5}$$

where m is the number of solid particles in the control volume, $\boldsymbol{x}_j$ is the coordinate of the mass center of the j-th solid particle, $\boldsymbol{v}_s$ is the velocity of solid particle, and $\boldsymbol{u}_f$ is the fluid velocity, which can be regarded as an averaged value of fluid velocity around the solid particle, equivalent to the velocity at the mass center as if the space occupied by the solid particle were filled with the fluid. β_j is the drag coefficient and V_j the volume of the j-th solid particle.

Similar to Eq. (2.5), we use the concentrated force to represent the resultant force due to the pressure on the solid particle surface, that is, we treat a solid particle either in one cell or another, but not in between. The pressure terms on the right hand side of Eq. (2.4) can be rewritten by using the divergence theorem as:

$$\begin{aligned}-\int_{\Sigma'\cup}p\boldsymbol{n}dA+\int_{A_p}p\boldsymbol{n}dA&=-\int_{\Sigma_1}p\boldsymbol{n}dA-\cdots-\int_{\Sigma_m}p\boldsymbol{n}dA=\int_{V_1}\nabla pdV+\cdots+\int_{V_m}\nabla pdV\\&\approx\nabla p(\boldsymbol{x}_1)V_1+\cdots+\nabla p(\boldsymbol{x}_m)V_m=\sum_{j=1}^{m}\nabla p\left(\boldsymbol{x}_j\right)V_j,\end{aligned} \tag{2.6}$$

https://doi.org/10.4208/cicp.OA-2016-0050 Published online by Cambridge University Press

where $\Sigma_1,\cdots,\Sigma_m$ are the surfaces of the solid particles.

Although the left side of Eq. (2.6) takes account of the solid particles crossing the border of the control volume, the right side contains only the whole particles, for all solid particles are treated either in one control volume or another, but not in between (This approach is just for the purpose of calculating the resultant force. The effect of the position of the solid particle mass center will be counted in the MPM, see Section 3). In this way the pressure term and the deviatoric stress term are treated consistently. The first term on the right hand side of Eq. (2.4) can be rewritten by applying the divergence theorem as

$$\int_{A_f\cup A_p}\boldsymbol{\sigma}\boldsymbol{n}dA=\int_V\nabla\cdot\boldsymbol{\sigma}dV. \tag{2.7}$$

Combining (2.2), (2.4) and (2.7), one gets

$$\int_V\theta\rho_f\frac{D\boldsymbol{u}_f}{Dt}dV=\int_V\theta\rho_f\boldsymbol{g}dV+\int_V\nabla\cdot\boldsymbol{\sigma}dV+\sum_{j=1}^m\nabla p\left(\boldsymbol{x}_j\right)V_j+\sum_{j=1}^m\beta_j\left(\boldsymbol{v}_s\left(\boldsymbol{x}_j\right)-\boldsymbol{u}_f\left(\boldsymbol{x}_j\right)\right)V_j. \tag{2.8}$$

To get the differential form of the governing equation, we use Dirac delta function to represent the distribution of the concentrated forces.

$$\sum_{j=1}^m\nabla p\left(\boldsymbol{x}_j\right)V_j=\int_V\sum_{j=1}^m\nabla p\left(\boldsymbol{x}\right)V_j\delta\left(\boldsymbol{x}-\boldsymbol{x}_j\right)dV, \tag{2.9}$$

$$\sum_{j=1}^m\beta_j\left(\boldsymbol{v}_s\left(\boldsymbol{x}_j\right)-\boldsymbol{u}_f\left(\boldsymbol{x}_j\right)\right)V_j=\sum_{j=1}^m\int_V\beta_j\left(\boldsymbol{v}_s\left(\boldsymbol{x}\right)-\boldsymbol{u}_f\left(\boldsymbol{x}\right)\right)V_j\delta\left(\boldsymbol{x}-\boldsymbol{x}_j\right)dV. \tag{2.10}$$

Substituting (2.9) and (2.10) into (2.8), we have

$$\begin{aligned}&\int_V\theta\rho_f\frac{D\boldsymbol{u}_f}{Dt}dV\\&=\int_V\left\{\theta\rho_f\boldsymbol{g}+\nabla\cdot\boldsymbol{\sigma}+\sum_{j=1}^m\left[\nabla p\left(\boldsymbol{x}\right)V_j\delta\left(\boldsymbol{x}-\boldsymbol{x}_j\right)+\beta_j\left(\boldsymbol{v}_s\left(\boldsymbol{x}\right)-\boldsymbol{u}_f\left(\boldsymbol{x}\right)\right)V_j\delta\left(\boldsymbol{x}-\boldsymbol{x}_j\right)\right]\right\}dV.\end{aligned} \tag{2.11}$$

Since the domain V in the above equation is arbitrary, to make two integrals equal we shall require the integrands on both sides equal. Thus we get the general form of governing equation in the differential form as follows

$$\theta\rho_f\frac{D\boldsymbol{u}_f}{Dt}=\theta\rho_f\boldsymbol{g}+\nabla\cdot\boldsymbol{\sigma}+\sum_{j=1}^M\left[\nabla p\left(\boldsymbol{x}\right)+\beta_j\left(\boldsymbol{v}_s-\boldsymbol{u}_f\right)\right]V_j\delta\left(\boldsymbol{x}-\boldsymbol{x}_j\right), \tag{2.12}$$

where M is the number of solid particles in the whole computational domain. If the interaction force from the solid phase is represented by $\boldsymbol{R}$, i.e. $\boldsymbol{R}=\sum_{j=1}^M[\nabla p(\boldsymbol{x})+\beta_j(\boldsymbol{v}_s-\boldsymbol{u}_f)]V_j\delta(\boldsymbol{x}-\boldsymbol{x}_j)$, Eq. (2.12) becomes the same form of momentum conservation equation of a continuous single phase derived in [36].

https://doi.org/10.4208/cicp.OA-2016-0050 Published online by Cambridge University Press

In the combined DEM-MPM, the motion of a solid particle is based on the resultant force the particle receives, including the contribution from the fluid field. The shear from the fluid is the reaction force of $\beta_j(\boldsymbol{v}_s(\boldsymbol{x}_j)-\boldsymbol{u}_f(\boldsymbol{x}_j))V_j$, and the pressure on a solid particle is the buoyance force, which can be calculated as

$$\int_{\Sigma_j} p\boldsymbol{n}dA=-\int_{V_j}\nabla p dV\approx -V_j\nabla p\left(\boldsymbol{x}_j\right), \tag{2.13}$$

where Σ_j and V_j are the surface and volume of the j-th solid particle, respectively.

The resultant force on fluid phase from the solid particle j is marked as $\boldsymbol{f}_f$, defined as

$$\boldsymbol{f}_f=V_j\left\{\nabla p\left(\boldsymbol{x}_j\right)+\beta_j\left[\boldsymbol{v}_s\left(\boldsymbol{x}_j\right)-\boldsymbol{u}_f\left(\boldsymbol{x}_j\right)\right]\right\}. \tag{2.14}$$

The average reaction force of the buoyance force (exerted on the fluid phase) per unit volume in the control volume can be estimated as follows, for the case in which the gradient of pressure is constant over each solid particle.

$$\frac{1}{V}\int_V\sum_{j=1}^m\nabla p(\boldsymbol{x})V_j\delta\left(\boldsymbol{x}-\boldsymbol{x}_j\right)dV=\frac{1}{V}\sum_{j=1}^m\nabla p\left(\boldsymbol{x}_j\right)V_j=\frac{\nabla p}{V}\sum_{j=1}^m V_j=\nabla p(1-\theta). \tag{2.15}$$

Here the locally averaged solid volume fraction over the control volume, $\frac{1}{V}\sum_{j=1}^m V_j=1-\theta$, is applied. Since $\sum_{j=1}^m\nabla p(\boldsymbol{x})V_j\delta(\boldsymbol{x}-\boldsymbol{x}_j)$ represents the force per unit volume, and has the same resultant force over the fluid inside the control volume, (i.e. $\nabla p(1-\theta)V$), in the case where the solid particles are very tiny and control volume is very small (so that the constant gradient of pressure would approximately hold. Mathematically, the gradient of pressure is independent of the location in the control volume as the control volume approaches infinitesimal). The Eq. (2.12) is thus rewritten as

$$\begin{aligned}\theta\rho_f\frac{D\boldsymbol{u}_f}{Dt}=&\theta\rho_f\boldsymbol{g}+\nabla\cdot\boldsymbol{\sigma}+\nabla p(1-\theta)+\sum_{j=1}^M\beta_j\left(\boldsymbol{v}_s-\boldsymbol{u}_f\right)V_j\delta\left(\boldsymbol{x}-\boldsymbol{x}_j\right)\\ =&\theta\rho_f\boldsymbol{g}-\theta\nabla p+\nabla\cdot\boldsymbol{\tau}+\sum_{j=1}^M\beta_j\left(\boldsymbol{v}_s-\boldsymbol{u}_f\right)V_j\delta\left(\boldsymbol{x}-\boldsymbol{x}_j\right).\end{aligned} \tag{2.16}$$

If $\boldsymbol{F}_f$ is used to represent the shear drag force per unit volume on fluid phase, which is the last term in the above equation, we get the exact same form of momentum equation as derived by Anderson and Jackson [39], though our derivation is much short and with fewer assumptions. In many applications, the shear drag force is actually calculated using formula (2.5), but an abstract symbol $\boldsymbol{F}_f$ or a term like $\beta(\boldsymbol{v}_s-\boldsymbol{u}_f)$ appears in the momentum conservation equation. The connection between $\boldsymbol{F}_f$ and the shear drag is missing. And, $\beta(\boldsymbol{v}_s-\boldsymbol{u}_f)$ does not reflect the essence of the empirical formula which basically is an estimate of a resultant force concentrated at the mass center. By using the Dirac delta function here, the nature of shear drag as an empirically determined resultant force concentrated at the mass point of dispersed solid phase is thus correctly represented in the momentum conservation equation.

https://doi.org/10.4208/cicp.OA-2016-0050 Published online by Cambridge University Press

2.3 Constitutive equations

The continuity equation (2.1) can be rewritten as

$$\frac{D\left(\theta\rho_f\right)}{Dt}=-\theta\rho_f\nabla\cdot\boldsymbol{u}_f, \tag{2.17}$$

where D/Dt denotes the substantial (material) derivative. Eq. (2.17) can be rewritten as

$$\frac{D\rho_f}{\rho_f Dt}=-\nabla\cdot\boldsymbol{u}_f-\frac{D\theta}{\theta Dt}. \tag{2.18}$$

In the Lagrangian description, $D\theta/Dt$ turns out to be $d\theta/dt$ which is the rate of change of fluid volume fraction of a given fluid particle, and $D\rho_f/Dt$ becomes $d\rho_f/dt$ which is the rate of change of fluid density. The fluid particle will be simulated using the MPM described in next section. The density ρ_f is the fluid particle density, not the density described at a fixed spatial point in the flow field in Eulerian description. In another word we will use Lagrangian description through this study.

Eq. (2.18) can be approximated by a finite difference form as

$$\frac{\Delta\rho_f}{\rho_f}=-\left(\nabla\cdot\boldsymbol{u}_f+\frac{1}{\theta}\frac{\Delta\theta}{\Delta t}\right)\Delta t=-\left(\Delta t\nabla\cdot\boldsymbol{u}_f+\frac{\theta-\theta_0}{\theta}\right), \tag{2.19}$$

where Δt is the time increment, and θ_0 is the fluid volume fraction at the previous time step.

The pressure change is related to the density change through bulk modulus in a linear relationship, i.e., $\Delta p=K\Delta\rho_f/\rho_f$, thus we have

$$\Delta p=-K\left(\Delta t\nabla\cdot\boldsymbol{u}_f+\frac{\theta-\theta_0}{\theta}\right). \tag{2.20}$$

The density of the fluid evolves from ρ_f^n at the previous time step to ρ_f^{n+1} at the current time step as

$$\rho_f^{n+1}=\frac{\rho_f^n}{1-\frac{p}{K}}. \tag{2.21}$$

Hence, the current fluid density may be roughly calculated from the current pressure p^{k+1} through $\rho_f^{n+1}=\frac{\rho_f^0}{1-(p^{n+1}/K)}$, where ρ_f^0 is the density in the initial condition and the initial pressure is assumed to be zero.

The deviatoric stress $\boldsymbol{\tau}$ is assumed to follow Navier-Poisson Law of a Newtonian fluid:

$$\boldsymbol{\tau}=2\eta\dot{\boldsymbol{\varepsilon}}_f^d, \tag{2.22}$$

where $\dot{\boldsymbol{\varepsilon}}_f^d$ is the deviatoric strain rate and η is the dynamic viscosity of the fluid.

https://doi.org/10.4208/cicp.OA-2016-0050 Published online by Cambridge University Press

2.4 The equation of solid particle motion

The motion of solid particles is considered at the level of each individual particle. The motion of mass center of each individual particle follows Newton's second law of motion for a single mass point, and the rotation of the particle follows Euler's Theorem, which is an extension of Newton's law to the motion of a rigid body.

$$m_s \frac{d\boldsymbol{v}_s}{dt} = \boldsymbol{f}_c - \boldsymbol{f}_f + m_s \boldsymbol{g}, \tag{2.23}$$

$$\boldsymbol{I}_c \frac{d\boldsymbol{\omega}_s}{dt} + \boldsymbol{\omega}_s \times (\boldsymbol{I}_c \boldsymbol{\omega}_s) = \boldsymbol{T}_c + \boldsymbol{T}_f, \tag{2.24}$$

where, m_s, $\boldsymbol{g}$, $\boldsymbol{f}_c$ are the mass of the solid particle, gravitational acceleration, and the reaction force due to contact (collision) with other solid particles or solid structures, respectively. The method for calculating $\boldsymbol{f}_c$ is the so called linear spring-dashpot model proposed by Cundall and Strack [40], where the spring is used for the elastic deformation while the dashpot accounts for the viscous dissipation and the damping factor is determined from a restitution coefficient provided. $\boldsymbol{I}_c$ is momentum of inertia relative to the particle mass center, and $\boldsymbol{\omega}_s$ is the angular velocity of the solid particle. $\boldsymbol{T}_c$ is the torque due to the contact force from other solid particles or solid structures. $\boldsymbol{T}_f$ is the torque due to the interaction with fluid phase. Because only force at the mass center of each solid particle is calculated, the torque relative to the mass center of the solid particle due to the interaction with fluid is neglected at the current model.

The motion of the solid particles is solved using the Discrete Element Method (DEM). The solid particle velocity and fluid velocity at the previous time step are used for calculating the shear drag at the current time step. The solid particle velocity is updated by solving the above equation. The angular velocity is used for calculating the shear force at the contact. The shear force is limited by applying Coulomb's friction law. The contact force is calculated based on the overlap between solid particles or solid structures using a viscous damped free vibration model. Further details can be found in the literature [6,40].

3 Discretization of governing equations

The material point method (MPM) is exploited to solve the above governing equations, in particular, the momentum balance equation (2.12).

Now we assume a trial function h in the form

$$h(\boldsymbol{x},t) = \sum_{j=1}^{N} h_j(t) S_j(\boldsymbol{x}), \tag{3.1}$$

where, $h_j(t)$ is a function of time and $S_j(\boldsymbol{x})$ a function of spatial coordinate. The trial function $h(\boldsymbol{x},t)$ consists of N products of these two basic functions. When this trial function is applied to an element of N nodes, $h_j(t)$ is the solution at j-th node varying with time, and $S_j(\boldsymbol{x})$ is the spatial interpolation function.

https://doi.org/10.4208/cicp.OA-2016-0050 Published online by Cambridge University Press

Multiplying (3.1) to (2.12), and then integrating the resulting equation over a computational domain Ω, one gets

$$\begin{aligned}
&\sum_{j=1}^{N} h_j(t) \int_\Omega \theta\rho_f \frac{D\boldsymbol{u}_f}{Dt} S_j(\boldsymbol{x}) dv \\
=&\sum_{j=1}^{N} h_j(t) \int_\Omega S_j(\boldsymbol{x}) \theta\rho_f \boldsymbol{g} dv + \sum_{j=1}^{N} h_j(t) \int_\Omega S_j(\boldsymbol{x}) \nabla\cdot\boldsymbol{\sigma} dv \\
&+\sum_{j=1}^{N} h_j(t) \int_\Omega S_j(\boldsymbol{x}) \left[\sum_{k=1}^{N_{sp}} \left[\nabla p(\boldsymbol{x}) + \beta_k \left(\boldsymbol{v}_s - \boldsymbol{u}_f \right) \right] V_k \delta(\boldsymbol{x}-\boldsymbol{x}_k) \right] dv,
\end{aligned} \tag{3.2}$$

where N_{sp} is the number of solid particles in domain Ω.

Now we introduce the material point method (MPM) by defining the mass of a fluid particle in a space ω as follows

$$M_p = \int_\omega \theta\rho_f d\omega. \tag{3.3}$$

The particle mass M_p never changes with time. It can also be regarded as $\theta V_\omega \rho_f$. The macro density is defined as the mass divided by the total volume, i.e. M_p/V_ω, which is equivalent to the product of micro density (material density) and volume fraction, shown as follows

$$\theta\rho_f = \frac{M_p}{V_\omega}. \tag{3.4}$$

Eq. (3.4) holds only if $\theta\rho_f$ is constant in space ω. This requirement can be avoided in the MPM, where, the mass of a material particle is treated as being concentrated at a point (that is why it is termed as the material point method). On the other hand, clearly,

$$\int_\omega M_p \delta\left(\boldsymbol{x}-\boldsymbol{x}_p^t\right) d\omega = M_p(\boldsymbol{x}_p^t), \tag{3.5}$$

where $\boldsymbol{x}_p^t$ is the coordinate of the material point at time t. Comparing (3.3) and (3.5), and considering that ω is arbitrary, we have

$$\theta\rho_f = M_p \delta\left(\boldsymbol{x}-\boldsymbol{x}_p^t\right). \tag{3.6}$$

In the case where there are N_p material particles inside the space Ω, by a similar argument, we have

$$\theta\rho_f = \sum_{p=1}^{N_p} M_p \delta\left(\boldsymbol{x}-\boldsymbol{x}_p^t\right). \tag{3.7}$$

The solution process of the momentum conservation equations will be significantly simplified by using the concept of the material point, as shown below.

https://doi.org/10.4208/cicp.OA-2016-0050 Published online by Cambridge University Press

Similar to the finite element method, the solution $\boldsymbol{u}_f(\boldsymbol{x},t)$ can be obtained through the interpolation of values at the nodes of a regular grid using shape functions:

$$\boldsymbol{u}_f(\boldsymbol{x},t)=\sum_{j=1}^{N_n}\boldsymbol{u}_{fj}(t)\,S_j(\boldsymbol{x}), \tag{3.8}$$

where N_n is the number of nodes in a grid cell (MPM mesh).

Substituting (3.7) into (3.2), one gets the left side

$$\begin{aligned}\sum_{j=1}^{N}h_j(t)\int_\Omega\theta\rho_f\frac{D\boldsymbol{u}_f}{Dt}S_j(\boldsymbol{x})\,d\Omega&=\sum_{j=1}^{N}h_j(t)\int_\Omega\sum_{p=1}^{N_p}M_p\delta\left(\boldsymbol{x}-\boldsymbol{x}_p^t\right)\frac{D\boldsymbol{u}_f}{Dt}S_j(\boldsymbol{x})\,d\Omega\\&=\sum_{j=1}^{N}h_j(t)\frac{d}{dt}\left[\sum_{p=1}^{N_p}M_p\boldsymbol{u}_f\left(\boldsymbol{x}_p^t,t\right)S_j\left(\boldsymbol{x}_p^t\right)\right]\\&=\sum_{j=1}^{N}h_j(t)\frac{d\overline{m\boldsymbol{u}}_{fj}}{dt},\end{aligned} \tag{3.9}$$

where

$$\overline{m\boldsymbol{u}}_{fj}=\sum_{p=1}^{N_p}M_p\boldsymbol{u}_f\left(\boldsymbol{x}_p^t,t\right)S_j\left(\boldsymbol{x}_p^t\right) \tag{3.10}$$

is the momentum of the fluid particle at grid node j, obtained by mapping momentum from material particles. The conversion from $D\boldsymbol{u}_f/Dt$ to $d\boldsymbol{u}_f/dt$ is because the fluid velocity is calculated at the point occupied by the moving fluid particle in Lagrangian description, not a fixed spatial point in Eulerian description.

Eq. (3.10) defines a mapping from particles in a cell to the grid nodes of the cell. This technique is also applied to locally calculate the averaged volume fraction of each phase at the grid nodes. The solid phase volume fraction and fluid phase volume fraction are calculated as follows.

$$\theta_{sj}=\frac{1}{V_j}\sum_{sp=1}^{N_{sp}}V_{sp}S_j\left(\boldsymbol{x}_{sp}^t\right), \tag{3.11}$$

$$\theta_j=\frac{1}{V_j}\sum_{p=1}^{N_p}\frac{M_p}{\rho_f}S_j\left(\boldsymbol{x}_p^t\right), \tag{3.12}$$

where the subscript sp represents the solid particle, V_{sp} is the volume of solid particle sp and V_j is the volume of all cells associated with the node j, given as

$$V_j=\int_\Omega S_j(\boldsymbol{x})\,d\Omega. \tag{3.13}$$

https://doi.org/10.4208/cicp.OA-2016-0050 Published online by Cambridge University Press

Because $\theta_{sj}+\theta_j=1$, the fluid volume fraction can be calculated from the solid particle volume fraction as follows,

$$\theta_j=1-\theta_{sj}. \tag{3.14}$$

As an inverse operation, the following mapping converts nodal variables to variables at the position of particles.

$$p(\boldsymbol{x},t)=\sum_{j=1}^{N_n}p_j(t)S_j(\boldsymbol{x}), \tag{3.15}$$

$$\theta(\boldsymbol{x},t)=\sum_{j=1}^{N_n}\theta_j(t)S_j(\boldsymbol{x}), \tag{3.16}$$

$$\boldsymbol{\sigma}(\boldsymbol{x},t)=\sum_{j=1}^{N_n}\boldsymbol{\sigma}_j(t)S_j(\boldsymbol{x}). \tag{3.17}$$

The first item on the right side of Eq. (3.2) is the gravitational force.

$$\int_\Omega\theta\rho_f\boldsymbol{g}S_j(\boldsymbol{x})d\Omega=\boldsymbol{g}\int_\Omega\sum_{p=1}^{N_p}M_p\delta\left(\boldsymbol{x}-\boldsymbol{x}_p^t\right)S_j(\boldsymbol{x})d\Omega=M_{pj}\boldsymbol{g}, \tag{3.18}$$

where

$$M_{pj}=\sum_{p=1}^{N_p}M_p\left(\boldsymbol{x}_p^t,t\right)S_j\left(\boldsymbol{x}_p^t\right) \tag{3.19}$$

is a mapping of mass from particles in a cell to the grid node of the cell.

The second item on the right side of Eq. (3.2) can be rewritten as

$$\int_\Omega S_j(\boldsymbol{x})\nabla\cdot\boldsymbol{\sigma}d\Omega=\int_S S_j(\boldsymbol{x})\boldsymbol{\sigma}\boldsymbol{n}ds-\int_\Omega\boldsymbol{\sigma}\nabla S_j(\boldsymbol{x})d\Omega. \tag{3.20}$$

The first term on the right side in the above is related to the boundary condition and is marked as

$$f_j^{bc}=\int_S S_j(\boldsymbol{x})\boldsymbol{\sigma}\boldsymbol{n}ds, \tag{3.21}$$

and the second term is the internal force

$$\begin{aligned}f_j^{int}&=-\int_\Omega\boldsymbol{\sigma}\nabla S_j(\boldsymbol{x})d\Omega=-\int_\Omega\rho_f\boldsymbol{\sigma}^s\nabla S_j(\boldsymbol{x})d\Omega=-\frac{1}{\theta}\int_\Omega\sum_{p=1}^{N_p}M_p\delta\left(\boldsymbol{x}-\boldsymbol{x}_p^t\right)\boldsymbol{\sigma}^s\nabla S_j(\boldsymbol{x})d\Omega\\&=-\frac{1}{\theta}\sum_{p=1}^{N_p}M_p\boldsymbol{\sigma}^s\left(\boldsymbol{x}_p^t\right)\nabla S_j\left(\boldsymbol{x}_p^t\right)=-\frac{1}{\theta}\sum_{p=1}^{N_p}\frac{M_p}{\rho_f}\boldsymbol{\sigma}_p\nabla S_j\left(\boldsymbol{x}_p^t\right),\end{aligned} \tag{3.22}$$

where, the specific stress $\boldsymbol{\sigma}^s=\boldsymbol{\sigma}/\rho_f$ is used in the derivation of Eq. (3.22). Eq. (3.7) is also applied to derive Eq. (3.22). Note that the fluid volume fraction is obtained by local averaging at the space Ω.

https://doi.org/10.4208/cicp.OA-2016-0050 Published online by Cambridge University Press

The last term in (3.2) is rewritten as:

$$\sum_{j=1}^{N} h_j(t) \int_{\Omega} S_j(\boldsymbol{x}) \left[\sum_{k=1}^{N_{sp}} \left[\nabla p(\boldsymbol{x}) + \beta_k \left(\boldsymbol{v}_s - \boldsymbol{u}_f \right) \right] V_k \delta(\boldsymbol{x} - \boldsymbol{x}_k) \right] d\Omega$$
$$= \sum_{j=1}^{N} h_j(t) \sum_{k=1}^{N_{sp}} \left[\nabla p(\boldsymbol{x}_k) + \beta_j \left(\boldsymbol{v}_s(\boldsymbol{x}_k) - \boldsymbol{u}_f(\boldsymbol{x}_k) \right) \right] S_j(\boldsymbol{x}_k) V_k, \tag{3.23}$$

where, V_k is the volume of solid particle k. Since the solid particles are regarded as rigid, the volume can be calculated either as $V_k = m_{sk}/\rho_{sk}$ or $V_k = (4/3)\pi r_{sk}^3$ if the particle is treated as a sphere, where m_{sk}, ρ_{sk} and r_{sk} are the mass, density and radius of the solid particle, respectively.

Let $\boldsymbol{f}_j^s$ be the interaction from the solid particles projected at node j.

$$\boldsymbol{f}_j^s = \sum_{k=1}^{N_{sp}} \left[\nabla p(\boldsymbol{x}_k) + \beta_j \left(\boldsymbol{v}_s(\boldsymbol{x}_k) - \boldsymbol{u}_f(\boldsymbol{x}_k) \right) \right] V_k S_j(\boldsymbol{x}_k). \tag{3.24}$$

The damping coefficient β is given by Ergun's equation [38] in the dense region and by Wen and Yu's equation [41] in the dilute region, as follows

$$\beta_k = \begin{cases} \frac{\eta(1-\theta)}{{d_{sk}}^2 \theta} [150(1-\theta) + 1.75Re], & \theta \le 0.8, \\ \frac{3}{4} C_D \frac{\eta(1-\theta)}{{d_{sk}}^2} \theta^{-2.7} Re, & \theta > 0.8, \end{cases} \tag{3.25}$$

where d_{sk} is the diameter of a solid particle k, and C_D is the drag coefficient and obtained using following expression

$$C_D = \begin{cases} 24\left(1 + 0.15 Re^{0.687}\right)/Re, & Re \le 1000, \\ 0.43, & Re > 1000, \end{cases} \tag{3.26}$$

where

$$Re = \frac{\left| \boldsymbol{v}_s(\boldsymbol{x}_k) - \boldsymbol{u}_f(\boldsymbol{x}_k) \right| \theta \rho_f d_{sk}}{\eta}. \tag{3.27}$$

A dimensionless parameter is advisable so that the viscosity and the particles size are removed from (3.25). In this way, a new parameter is defined

$$\beta_k' = \begin{cases} \frac{(1-\theta)}{\theta} [150(1-\theta) + 1.75Re], & \theta \le 0.8, \\ \frac{3}{4} C_D (1-\theta) \theta^{-2.7} Re, & \theta > 0.8. \end{cases} \tag{3.28}$$

Accordingly, Eq. (3.24) is rewritten as

$$\boldsymbol{f}_j^s = \sum_{k=1}^{N_{sp}} \left[\nabla p(\boldsymbol{x}_k) + \frac{\eta}{{d_{sk}}^2} \beta_k' \left(\boldsymbol{v}_s(\boldsymbol{x}_k) - \boldsymbol{u}_f(\boldsymbol{x}_k) \right) \right] V_k S_j(\boldsymbol{x}_k). \tag{3.29}$$

https://doi.org/10.4208/cicp.OA-2016-0050 Published online by Cambridge University Press

For sphere solid particles, $V_k=(\pi/6){d_{sk}}^3$

$$\boldsymbol{f}_j^s=\sum_{k=1}^{N_{sp}}\left[\nabla p(\boldsymbol{x}_k)V_k+\frac{\pi d_{sk}}{6}\eta\beta_k'\left(\boldsymbol{v}_s(\boldsymbol{x}_k)-\boldsymbol{u}_f(\boldsymbol{x}_k)\right)\right]S_j(\boldsymbol{x}_k). \tag{3.30}$$

Therefore, equation (3.2) can be rewritten as

$$\sum_{j=1}^{N}h_j(t)\frac{d\overline{m\boldsymbol{u}}_{fj}}{dt}=\sum_{j=1}^{N}h_j(t)\left(M_{pj}\boldsymbol{g}+\boldsymbol{f}_j^{bc}+\boldsymbol{f}_j^{int}+\boldsymbol{f}_j^s\right). \tag{3.31}$$

Since $\sum_{j=1}^{N}h_j(t)$ is arbitrary, we have

$$\frac{d\overline{m\boldsymbol{u}}_{fj}}{dt}=M_{pj}\boldsymbol{g}+\boldsymbol{f}_j^{bc}+\boldsymbol{f}_j^{int}+\boldsymbol{f}_j^s=\boldsymbol{f}_j. \tag{3.32}$$

Given $\overline{m\boldsymbol{u}}_{fj}{}^{n+1}$ and $\overline{m\boldsymbol{u}}_{fj}{}^{n}$ the moment at two consecutive time steps, we have

$$\overline{m\boldsymbol{u}}_{fj}{}^{n+1}\approx\overline{m\boldsymbol{u}}_{fj}{}^{n}+\Delta t\boldsymbol{f}_j{}^{n}. \tag{3.33}$$

Eq. (3.33) is the MPM formula used for solving the momentum equation (2.12). It is a general form and has been applied to solve momentum equation in many applications (e.g. [21, 34]). To obtain convergent solutions, the time step must follow the stability condition. It is recommended to use time step that is one tenth of the period in which sound wave passes through the cell. Artificial lower sound wave speed (artificial lower density of the fluid) may be explored to achieve high computational efficiency in practice.

Once the new momentum at the nodes becomes known, the velocity at the nodes can be updated as

$$\boldsymbol{u}_{fj}{}^{n+1}=\frac{\overline{m\boldsymbol{u}}_{fj}{}^{n+1}}{M_j}. \tag{3.34}$$

Then the fluid material point velocity is updated as

$$\boldsymbol{u}_f{}^{n+1}=\sum_{j=1}^{N_n}\boldsymbol{u}_{fj}{}^{n+1}S_j\left(\boldsymbol{x}_p^t\right). \tag{3.35}$$

The nodal acceleration is updated as

$$\boldsymbol{a}_j{}^{n+1}=\frac{f_j{}^{n+1}}{M_j}, \tag{3.36}$$

and the acceleration of the fluid particle is updated as

$$\boldsymbol{a}_p{}^{n+1}=\sum_{j=1}^{N_n}\boldsymbol{a}_j{}^{n+1}S_j\left(\boldsymbol{x}_p^t\right). \tag{3.37}$$

https://doi.org/10.4208/cicp.OA-2016-0050 Published online by Cambridge University Press

The strain rate tensor, stress tensor will be updated based on the fluid velocity $\bar{\boldsymbol{u}}_f^{n+1}$, which is calculated from the fluid particle acceleration,

$$\bar{\boldsymbol{u}}_f^{n+1} = \boldsymbol{u}_f{}^n + \boldsymbol{a}_p{}^{n+1}\Delta t. \tag{3.38}$$

The updated position of the fluid particle is calculated as

$$\boldsymbol{x}_f{}^{n+1} = \boldsymbol{x}_f{}^n + \boldsymbol{u}_f{}^{n+1}\Delta t. \tag{3.39}$$

Note the operation for updating the fluid particle coordinate will not be done until the calculation of interaction force (contact force) for the solid particle is finished, because the position should all be at the previous time step in order to calculate the forces for both fluid particles and solid particles based upon the known positions. This algorithm is called modified update stress last (MUSL) [42].

4 Verification and validation

In order to accurately predict a process using numerical methods, a new code must pass verification and validation. Code verification is a prerequisite to code validation. The former one requires that the code is correct, mathematically. If there exists an analytic solution, the code should be able to produce a numerical result that approximates to the analytic solution in a certain convergence rate. The latter one requires that the code can reproduce the numerical result that is close to the result of physical experiments. Once the code passes the validation, the confidence to predict the real world events is then established.

Though there are many issues around the DEM, the confidence in using DEM to simulate multi-body motion is widely established in industries [3]. Thus we will not address the verification and validation of the DEM in this paper, instead, we focus our attention on the verification and validation of the MPM in the simulation of multiphase fluid motion. So far the analytical solution of a multiphase flow problem has not been found. Our stratagem of code verification is to try many different cases and check if the model predictions are correct in mathematics and in physics. For example, when the volume fraction is assumed to be 100%, the multiphase model actually becomes a single phase model, therefore, the new code should be able to reproduce the results of a single phase experiment. Models of varying size of background mesh put the MPM-DEM on the convergence test. These tests are not a sufficient condition to approve the code, but a very useful step in the code development. Further validation is completed in another test in which both solid phase and fluid phase are presented.

4.1 Water flow after reservoir dam breakage

First we compare our result with that obtained by Mast, Mackenzie-Helnwein et al. [43] simply because we adopt similar stratagem and there are experimental data available in [44].

https://doi.org/10.4208/cicp.OA-2016-0050 Published online by Cambridge University Press

A simplified dam break is sketched in Fig. 2. A water column of initial height, h_0, and length, l_0, is initially constrained horizontally and rests on a smooth, flat surface. The dynamic code is run about 0.3 second to allow the static pressure field being stabilized. Now we mark the time $t=0$ when the gate on the right-hand side is removed and the water is allowed to flow freely under the force of gravity. The following parameters describe the free surface run out:

$$T=t\sqrt{\frac{h_0 g}{{l_0}^2}}, \qquad L(T)=\frac{l(T)}{l_0}, \quad \text{and} \quad H(T)=\frac{h(T)}{h_0}, \tag{4.1}$$

where T, $L(T)$ and $H(T)$ are the dimensionless time, length, and height ratios, respectively. The parameters h_0 and l_0 are 4.0 meters each. The term $g=|\boldsymbol{g}|=9.8\ m/s^2$. The viscosity of water is taken as 0.001 Pas. There are $2\times2\times1$ particles in each cell initially. The physical experiment is basically a 2D case. Our numerical model takes a thin slice in 3D space of 4 meter high and 24 meter long. The thickness of this slice is the size of a fluid particle. The initial configuration of the water column is of square shape with length of 4 meters, which can be divided into regular meshes. The rest domain is divided into regular meshes of the same size. The cell resolution is 0.125 meter in length, 0.125 meter in height and 0.0625 meter in thickness for model MPM32. Table 1 summarizes the parameters used in the numerical tests.

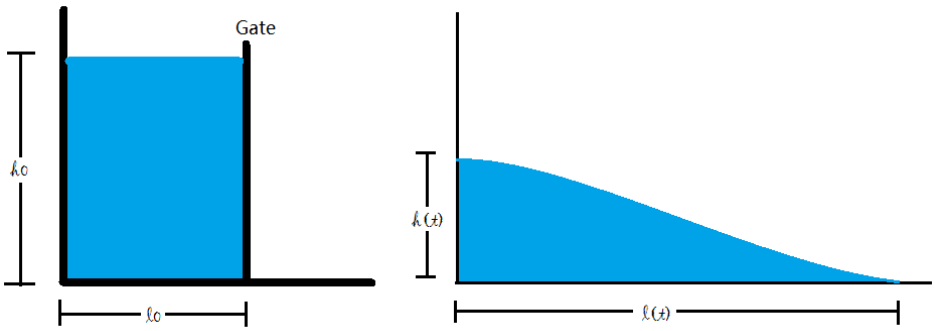


Figure 2: Dam breakage simulation.

The predictions from the MPM is shown in Fig. 3 by a series of snaps taken at time $T=0$, 0.5, 1.0, 1.5, 2.0,2.5, 3.0. It is observed that water surface tilting and the right corner flowing out. The water flow predicted from the MPM model is comparable with that by Mast, Mackenzie-Helnwein et al. [43].

The quantitative comparison between the model predictions and experimental data are shown in Fig. 4. In Fig. 4A, the predictions from a MPM model with free-slip and non-slip boundary conditions are given, respectively. The former one is marked as MPM1 and the latter one as MPM2. The MPM1 predicts the result which is identical to that

https://doi.org/10.4208/cicp.OA-2016-0050 Published online by Cambridge University Press

Table 1: Physical properties and computational parameters.

Item	value
Water column initial height (m)	4.0
Water column initial length (m)	4.0
MPM mesh cell size (m)	Varying from 0.125 to 0.25
Initial Number of particle per cell	$2\times2\times1$
Density (kg/m^3)	1000
Bulk modulus (Pa)	2.2e9
Dynamic viscosity (Pas)	0.001
Time step (s)	1.0e-5

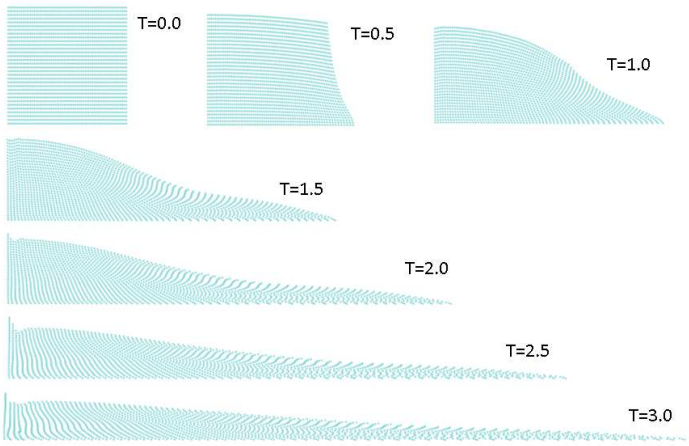


Figure 3: Dam breakage sequence predicted from a MPM simulation.

by Mast, Mackenzie-Helnwein et al. [43]. This is understandable because we use the cell-based anti-locking technique as they did. Note that the predicted length is larger than the length from the experimental data. The MPM2 gives a much better fit to the experimental data. It is reasonable that free-slip boundary condition promotes the flow while non-slip boundary condition represents the physical condition better.

The resolution of the MPM grid is another factor that may affect the model predictions. The Fig. 4B shows the predictions from three MPM models. There are 16 cells in the length of initial length 4.0 m in the model MPM16, and 24 in MPM24, and 32 in MPM32. It is very clear from Fig. 4B that the prediction becomes better and better as the spatial resolution improves.

The height history predicted from these models is also shown in Fig. 4(C and D). Generally, they are comparable with the experimental data. Larger error happens at the $T>2.5$ when the water layer becomes very thin (see Fig. 3).

https://doi.org/10.4208/cicp.OA-2016-0050 Published online by Cambridge University Press

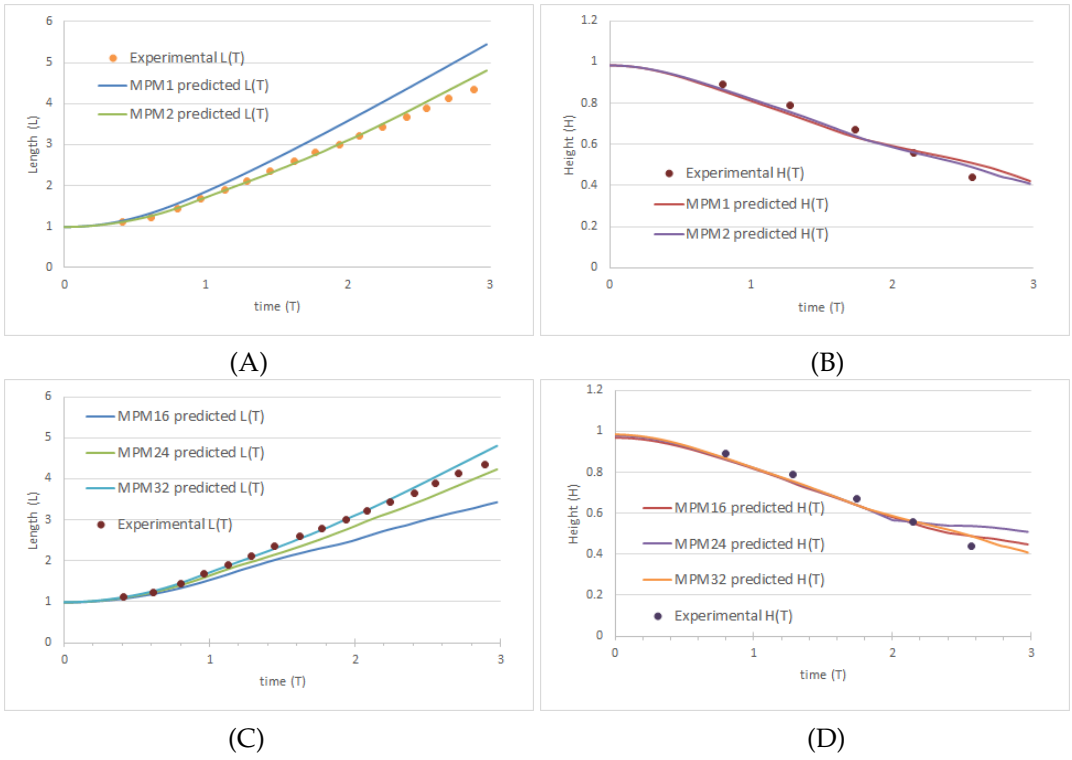


Figure 4: Comparison between MPM simulation and experimental data for dam breakage model.

Both visual and quantitative comparisons show the cell-based implementations in our code are successful, but this only shows our code can be used for the simulation of pure fluid case. We need to demonstrate more examples to show the success of our method in the multiphase flow.

4.2 Motion of glass beads and water in a tank

Here we demonstrate a case very similar to the water dame breakage, however, this time there is a solid phase-glass beads mingled with water inside the rectangular tank. This case is presented in the research paper by Sun et al. [18]. For the readers' convenience, a brief description is given below.

The mixture of water and glass beads has an altitude of 0.1 m. The mass of glass beads is 200 gram and the density is 2500 kg/m^3. The diameter of the beads is 2.7 mm. The dimensions of the tank are 0.2 m in length, 0.1 m in width and 0.15 m in altitude. The mixture is contained in the left side with the gate being set at 0.05 m from the left side wall of the tank. Time starts at the moment when the gate is raised at a rate of 0.68 m/s. The stiffness, restitution coefficient and friction coefficient of the solid particles are chosen as 1000 N/m, 0.9 and 0.2, respectively, same as those used in SPH-DEM simulation by Sun

https://doi.org/10.4208/cicp.OA-2016-0050 Published online by Cambridge University Press

Table 2: Physical properties and computational parameters.

Item	value
Solid phase	
DEM particle number	7762
Particle diameter (m)	0.0027
Density (kg/m^3)	2.5e3
Stiffness (N/m)	1.0e3
Restitution coefficient	0.9
Friction coefficient	0.2
Liquid phase	
MPM particle number	26,879
MPM mesh cell size (m)	0.005
Initial Number of particle per cell	$2\times2\times2$
Density (kg/m^3)	1000
Dynamic viscosity (Pas)	0.001
Virtual bulk modulus (Pa)	2.2e7
Solid structural boundary	
Dimensions (m)	$0.2\times0.1\times0.15$
Number of triangle meshes	22
Gate rising rate (m/s)	0.68

et al. [18]. Non-slip boundary condition is applied where water contacts the walls and the bottom of the tank. A fixed time increment of 1.0×10^{-5} s is used throughout the simulation. We simulate water with 26879 material particles and the background mesh of 0.005 m resolution. The physical and model parameters are listed in Table 2.

We first prepare settled configuration of the mixture before the gate being raised, and then simulate the process of two-phase flow. Fig. 5 shows four snapshots of the result from the simulation, for selected time instants of $t=0.05$, 0.1, 0.15 and 0.2 s. And quantitative comparison with experimental data is presented in Fig. 6. It is observed that the solid particles fall a little bit behind the water front, consistent with the experimental data. Quantitative comparison in Fig. 6 gives us sufficient evidence that the proposed DEM-MPM method is capable of making prediction with high fidelity.

4.3 Solid-fluid flow in a rotating jar

Our original idea is to validate the new method with more experimental data. The case of solid-fluid flow in a rotating jar presented by Sun et al. [18] is chosen for this purpose. Because no boundary condition is described, we simply apply non-slip condition on the wall of the jar whenever the fluid contacts. It turns out this model is unable to reproduce what it is observed in the experiment.

https://doi.org/10.4208/cicp.OA-2016-0050 Published online by Cambridge University Press

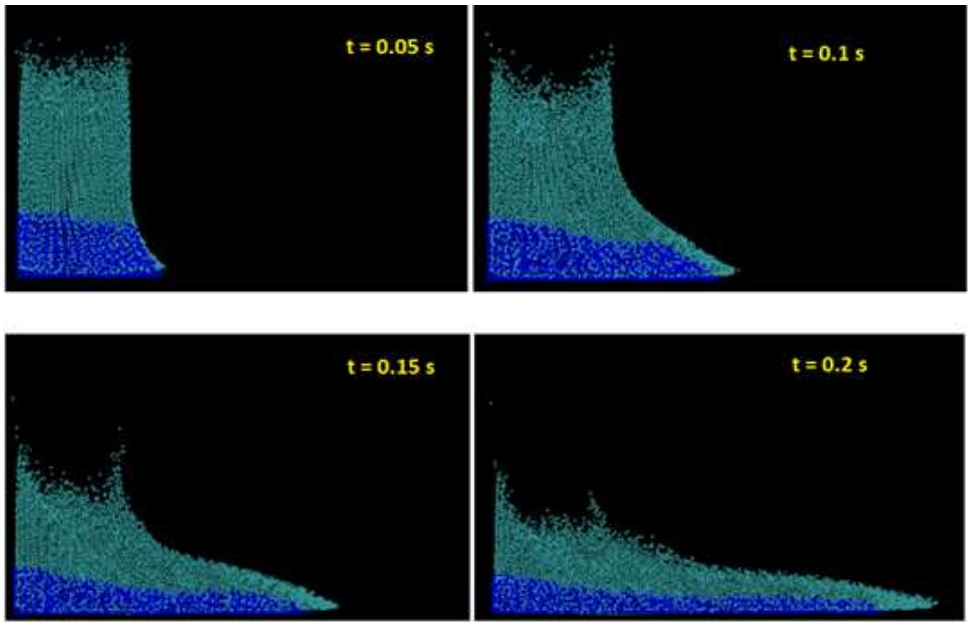
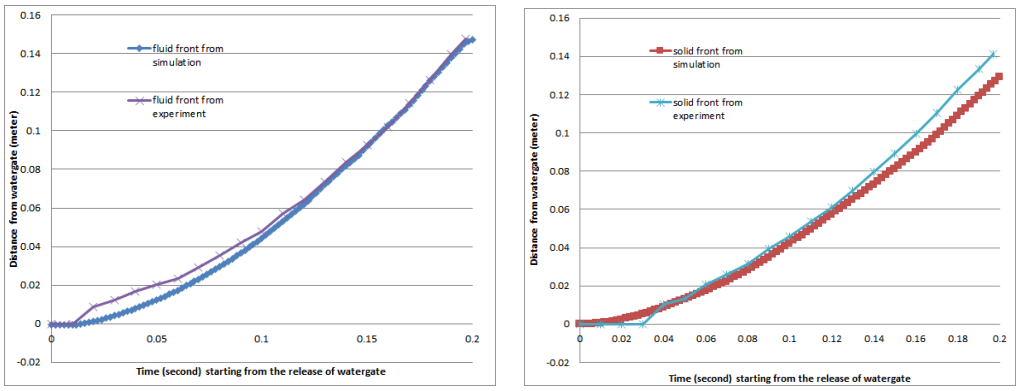


Figure 5: Simulation of two-phase flow in a tank, 4 snapshots from numerical modeling. The dark blue dots stand for the glass beads, while light blue dots for water.



(A) (B)

Figure 6: Comparison between numerical results and experimental data for two-phase flow.

This model simulates the solid-fluid flow in a cylindrical jar with both inner diameter and depth being 100 mm. The jar contains 7755 solid spherical particles (glass beads) with diameter 2.7 mm and density 2700 kg/m^3. It also contains 0.297 kg of water with density 1000 kg/m^3 and viscosity 0.001 Pas. The jar rotates at the rate of 104 revolutions per minute. The DEM is exploited to simulate the glass beads, and the stiffness, restitution coefficient and friction coefficient are set to be 1000 N/m, 0.8 and 0.3, respectively. The MPM is for fluid phase with 15406 particles of identical fluid mass. There are $36\times36\times10$

https://doi.org/10.4208/cicp.OA-2016-0050 Published online by Cambridge University Press

Table 3: Physical properties and computational parameters.

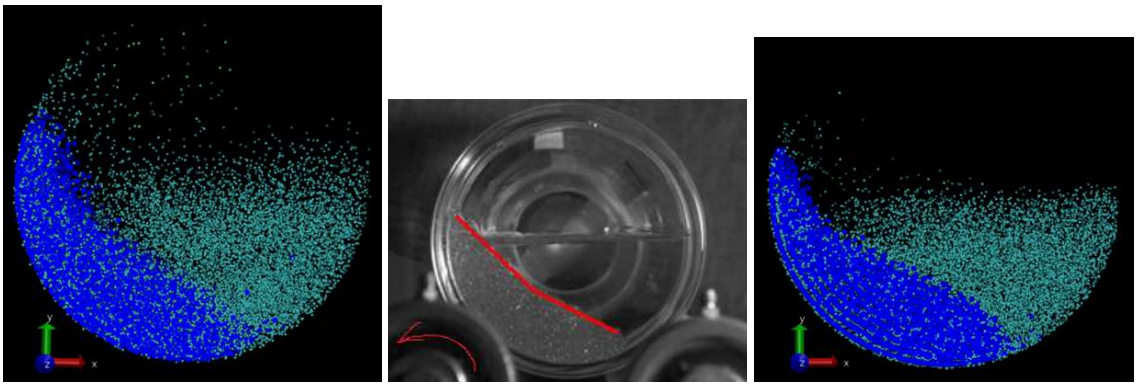
Item	value
Solid phase	
DEM particle number	7755
Particle diameter (m)	2.7e3
Density (kg/m^3)	2.5e3
Stiffness (N/m)	1.0e3
Restitution coefficient	0.9
Friction coefficient	0.3
Liquid phase	
MPM particle number	15,406
MPM mesh cell size (m)	0.00278
Initial Number of particle per cell	$2\times2\times2$
Density (kg/m^3)	1000
Dynamic viscosity (Pas)	0.001
Virtual bulk modulus (Pa)	2.2e7
Solid structural boundary	
Number of triangle meshes	1440
Rotation speed (rpm)	104

cells evenly distributed in 100 mm $\times$ 100 mm $\times$ 100 mm cubic space with $1\times1\times4$ MPM particles in each cell when the cell is full of fluid particles at the initial condition. The interior surfaces of the jar are simulated with 1440 triangles. These parameters for the simulation are listed in Table 3.

Because of the constant rotating rate, the configuration of the glass beads inside the jar will take a stable shape after a certain period of transition. The configuration of the beads is measured and simulated. In the experiment, the maximum altitude of the beads in the stable state is 62.18 mm in average with standard deviation 1.71 mm. In the simulation with non-slip boundary condition applied, the model predicted maximum altitude in bead bed is 67 mm. We also noticed that the water particles diffuse over space inside the jar. There is no clear free surface observed. The comparison is shown in Fig. 7(A) and (B).

What causes this difference? We notice the difference in the first case of pure water flow and the influence of boundary condition. Strictly speaking, non-slip boundary condition and free-slip condition are two end-member in describing the interaction between the boundary and the interior mass. Non-slip boundary works better in the case of low Reynolds number while free-slip for the large Reynolds number. In reality, the interaction may exist between the two end-member conditions. In the case using non-slip boundary condition, the boundary has the strongest coupling with the interior mass. This is the case for rotating jar: when non-slip boundary condition is applied, more energy is transferred from boundary wall to the interior mass including glass beads and water. The

https://doi.org/10.4208/cicp.OA-2016-0050 Published online by Cambridge University Press



(A) (B) (C)

Figure 7: Comparison between numerical results and physical experiment for rotating jar. The dark blue dots stand for the glass beads, while light blue dots for water. A) Model with non-slip boundary condition; B) Stable state of beads and water in a rotating jar in physical experiment (based on Sun et al. [18]); C) Models with 50% of sticky boundary condition.

lifting force is high and the final balanced altitude is higher than the real value observed in the laboratory.

A reasonable guess is that the boundary may partially sticky (non-slip) and partially slippery (free slip). To check this hypothesis, we tested a case in which 50% of the boundary velocity is sticky and the rest is slippery. The result is shown in Fig. 7(C). It is obvious that the simulation fits the experiment result much better. The water particles form a clear free surface and the maximum altitude in bead bed is 61 mm. In the case water is full in the rotating jar, the Reynolds number could be estimated up to 2×10^7, much higher than the value for the laminate flow in which non-slip boundary is justified. How to find a proper boundary condition for high Reynolds number flow is something we should continue to explore. The comparison shown in this case highlights the importance of boundary condition in fidelity of numerical modeling.

The combined MPM-DEM method developed in this study applies for the interaction among solid discrete elements and the fluid in between. Theoretically it works for both liquid saturated or unsaturated and gas. So far we have verified that it works for liquid, further verification is required for gas. The proposed MPM-DEM method is far from perfect. In this method the MPM cell is required to be larger than the size of solid particles. In an industrial application like a sieve, in which small particles are allowed to pass but big particles (compared with sieve size) are not, the accuracy of this method and the applicability of this method is a problem. Future study in this direction is in need.

5 Conclusions

In this study, a combined DEM-MPM method is proposed and demonstrated for the simulation of multiphase flow. By applying Newton's law of motion on the fluid phase,

https://doi.org/10.4208/cicp.OA-2016-0050 Published online by Cambridge University Press

we derive the equation of momentum conservation, which is consistent with the existing equation. However, our derivation is much shorter and has fewer assumptions. The fluid motion and the interaction between the solid phase and fluid are simulated using the MPM, while the contact forces between solid particles and solid structure are calculated using the DEM. Due to the nature of the MPM, the free surface of the fluid is naturally formed without invoking any special treatment.

The proposed method is verified and validated using both experimental data and similar numerical tests. The reduced form of the model is validated in a water flow experiment, and the full scale solid-liquid interaction is validated in a water-glass beads mixture flow test. The dynamic behavior of fluid head is well reproduced in the numerical simulation. The quantitative comparison shows the consistency with previous numerical results and with physical experiments. The simulation results obtained with the proposed method also demonstrate the effects of spatial resolution and boundary condition on the fidelity of numerical simulation. Thus, we have shown that the combined DEM-MPM method is effective in simulating a certain type of solid-liquid flow problems. However, much research remains to be performed to verify and validate the proposed procedure for general engineering applications.

Acknowledgments

P. Sun was partially supported by NSF Grant DMS-1418806. Figs. 3, 5 and 7 are prepared by using VMD [45].

References

[1] R. Sun and H. Xiao, Diffusion-based coarse graining in hybrid continuum-discrete solvers: Applications in CFD-DEM, International Journal of Multiphase Flow, vol. 72, pp. 233-247, 2015.
[2] N. S. Weerasekara, M. S. Powell, P. W. Cleary, L. M. Tavares, M. Evertsson, R. D. Morrison, et al., The contribution of DEM to the science of comminution, Powder Technology, vol. 248, pp. 3-4, 2013.
[3] H. P. Zhu, Z. Y. Zhou, R. Y. Yang, and A. B. Yu, Discrete particle simulation of particulate systems: Theoretical developments, Chemical Engineering Science, vol. 62, pp. 3378-3396, 2007.
[4] C. S. Campbell, Computer Simulation of Rapid Granular Flows, in Proceedings of the U.S. National Congress of Applied Mechanics, 1986, pp. 327-338.
[5] Y. Yamada and M. Sakai, Lagrangian-Lagrangian simulations of solid-liquid flows in a bead mill, Powder Technology, vol. 239, pp. 105-114, 2013.
[6] Y. Tsuji, T. Kawaguchi, and T. Tanaka, Discrete particle simulation of two-dimensional fluidized bed, Powder Technology, vol. 77, pp. 79-87, 1993.
[7] K. W. Chu, B. Wang, A. B. Yu, and A. Vince, CFD-DEM modelling of multiphase flow in dense medium cyclones, Powder Technology, vol. 193, pp. 235-247, 2009.
[8] K. W. Chu and A. B. Yu, Numerical simulation of complex particle-fluid flows, Powder Technology, vol. 179, pp. 104-114, 2008.

https://doi.org/10.4208/cicp.OA-2016-0050 Published online by Cambridge University Press

[9] T. Kawaguchi, T. Tanaka, and Y. Tsuji, Numerical simulation of two-dimensional fluidized beds using the discrete element method (comparison between the two- and three-dimensional models), Powder Technology, vol. 96, pp. 129-138, 1998.
[10] M. Robinson, M. Ramaioli, and S. Luding, Fluid-particle flow simulations using two-way-coupled mesoscale SPH-DEM and validation, International Journal of Multiphase Flow, vol. 59, pp. 121-134, 2014.
[11] A. V. Potapov, M. L. Hunt, and C. S. Campbell, Liquid-solid flows using smoothed particle hydrodynamics and the discrete element method, Powder Technology, vol. 116, pp. 204-213, 2001.
[12] J. J. Monaghan, An introduction to SPH, Computer Physics Communications, vol. 48, pp. 89-96, 1988.
[13] J. J. Monaghan, Smoothed particle hydrodynamics, Annual Review of Astronomy and Astrophysics, vol. 30, pp. 543-574, 1992.
[14] M. Sinnott, P. W. Cleary, and R. D. Morrison, Slurry flow in a tower mill, Minerals Engineering, vol. 24, pp. 152-159, 2011.
[15] D. Gao and J. A. Herbst, Alternative ways of coupling particle behaviour with fluid dynamics in mineral processing, International Journal of Computational Fluid Dynamics, vol. 23, pp. 109-118, 2009.
[16] P. W. Cleary, Prediction of coupled particle and fluid flows using DEM and SPH, Minerals Engineering, vol. 73, pp. 85-99, 2015.
[17] K. W. Chu, S. B. Kuang, A. B. Yu, and A. Vince, Particle scale modelling of the multiphase flow in a dense medium cyclone: Effect of fluctuation of solids flowrate, Minerals Engineering, vol. 33, pp. 34-45, 2012.
[18] X. Sun, M. Sakai, and Y. Yamada, Three-dimensional simulation of a solid-liquid flow by the DEM-SPH method, Journal of Computational Physics, vol. 248, pp. 147-176, 2013.
[19] W. Dehnen and H. Aly, Improving convergence in smoothed particle hydrodynamics simulations without pairing instability, Monthly Notices of the Royal Astronomical Society, vol. 425, pp. 1068-1082, 2012.
[20] T. Belytschko, Y. Guo, W. K. Liu, and S. P. Xiao, A unified stability analysis of meshless particle methods, International Journal for Numerical Methods in Engineering, vol. 48, pp. 1359-1400, 2000.
[21] D. Sulsky, Z. Chen, and H. L. Schreyer, A particle method for history-dependent materials, Computer Methods in Applied Mechanics and Engineering, vol. 118, pp. 179-196, 1994.
[22] Y. Lian, F. Zhang, Y. Liu, and X. Zhang, Material point method and its applications, Advances in Mechanics, vol. 43, pp. 237-264, 2013.
[23] S. Bandara and K. Soga, Coupling of soil deformation and pore fluid flow using material point method, Computers and Geotechnics, vol. 63, pp. 199-214, 2015.
[24] P. Liu, Y. Liu, X. Zhang, and Y. Guan, Investigation on high-velocity impact of micron particles using material point method, International Journal of Impact Engineering, vol. 75, pp. 241-254, 2015.
[25] H. W. Zhang, K. P. Wang, and Z. Chen, Material point method for dynamic analysis of saturated porous media under external contact/impact of solid bodies, Computer Methods in Applied Mechanics and Engineering, vol. 198, pp. 1456-1472, 2009.
[26] A. R. York Ii, D. Sulsky, and H. L. Schreyer, Fluid-membrane interaction based on the material point method, International Journal for Numerical Methods in Engineering, vol. 48, pp. 901-924, 2000.
[27] P. Mackenzie-Helnwein, P. Arduino, W. Shin, J. A. Moore, and G. R. Miller, Modeling strate-

https://doi.org/10.4208/cicp.OA-2016-0050 Published online by Cambridge University Press

gies for multiphase drag interactions using the material point method, International Journal for Numerical Methods in Engineering, vol. 83, pp. 295-322, 2010.
[28] D. Z. Zhang, Q. Zou, W. B. VanderHeyden, and X. Ma, Material point method applied to multiphase flows, Journal of Computational Physics, vol. 227, pp. 3159-3173, 2008.
[29] L. T. Tran, J. Kim, and M. Berzins, Solving time-dependent PDEs using the material point method, a case study from gas dynamics, International Journal for Numerical Methods in Fluids, vol. 62, pp. 709-732, 2010.
[30] Z. Chen, L. Shen, Y. W. Mai, and Y. G. Shen, A bifurcation-based decohesion model for simulating the transition from localization to decohesion with the MPM, Zeitschrift fur Angewandte Mathematik und Physik, vol. 56, pp. 908-930, 2005.
[31] Y. Gan, Z. Chen, and S. Montgomery-Smith, Improved material point method for simulating the zona failure response in piezo-assisted intracytoplasmic sperm injection, Computer Modeling in Engineering and Sciences, vol. 73, pp. 45-75, 2011.
[32] X. Zhang, K. Y. Sze, and S. Ma, An explicit material point finite element method for hypervelocity impact, International Journal for Numerical Methods in Engineering, vol. 66, pp. 689-706, 2006.
[33] S. Mao, Material point method and adaptive meshing applied to fluid-structure interaction (FSI) problems, in American Society of Mechanical Engineers, Fluids Engineering Division (Publication) FEDSM, 2013.
[34] S. Jiang, Z. Chen, T. D. Sewell, and Y. Gan, Multiscale simulation of the responses of discrete nanostructures to extreme loading conditions based on the material point method, Computer Methods in Applied Mechanics and Engineering, vol. 297, pp. 219-238, 2015.
[35] Z. Jin, Y. Yuan, and M. Song, Interior Ballistics: Beijing Institute of Technology Press, 1992.
[36] C. E. Brennen, Fundamentals of Multiphase Flows: Cambridge University Press, 2005.
[37] T. Kawaguchi, T. Tanaka, and Y. Tsuji, Numerical simulation of two-dimensional fluidized beds using DEM (The case of spouted bed: Comparison between 2-D model and 3-D model), Nippon Kikai Gakkai Ronbunshu, B Hen/Transactions of the Japan Society of Mechanical Engineers, Part B, vol. 61, pp. 3169-3175, 1995.
[38] S. Ergun, Fluid flow through packed columns, Chemical Engineering and Processing, vol. 48, pp. 89-94, 1952.
[39] T. B. Anderson and R. Jackson, A fluid mechanical description of fluidized beds: Equations of motion, Industrial and Engineering Chemistry Fundamentals, vol. 6, pp. 527-539, 1967.
[40] P. A. Cundall and O. D. L. Strack, A discrete numerical model for granular assemblies, Geotechnique, vol. 29, pp. 47-65, 1979.
[41] C. Y. Wen and Y. H. Yu, Mechanics of fluidization, A.I.Ch.E. Series, vol. 62, pp. 100-111, 1966.
[42] O. Buzzi, D. M. Pedroso, and A. Giacomlnl, Caveats on the implementation of the generalized material point method, Computer Modeling in Engineering and Sciences, vol. 31, pp. 85-106, 2008.
[43] C. M. Mast, P. Mackenzie-Helnwein, P. Arduino, G. R. Miller, and W. Shin, Mitigating kinematic locking in the material point method, Journal of Computational Physics, vol. 231, pp. 5351-5373, 2012.
[44] J. Martin and W. Moyce, An experimental study of the collapse of liquid columns on a rigid horizontal plane, Philosophical Transactions of the Royal Society of London, vol. 244, pp. 312-324, 1952.
[45] W. Humphrey, A. Dalke, and K. Schulten, VMD – Visual molecular dynamics, Journal of Molecular Graphics, vol. 14, pp. 33-38, 1996.

https://doi.org/10.4208/cicp.OA-2016-0050 Published online by Cambridge University Press